

Detection of Enhanced Germanium in a New Cool Extreme Helium Star A 980: Insights and Implications

AJAY KUMAR SAINI ^{1,2} AND GAJENDRA PANDEY ¹

¹Indian Institute of Astrophysics, II Block, Koramangala, Bengaluru-560034, Karnataka, India

²Pondicherry University, R.V. Nagar, Kalapet, Pondicherry-605014, UT of Puducherry, India

ABSTRACT

A fine abundance analysis of a recently discovered hydrogen-deficient carbon (HdC) star, A 980, is presented. Based on the observed high-resolution optical spectrum, we ascertain that A 980 is a cool extreme helium (EHe) star and not an HdC. Singly-ionized germanium Ge II lines are identified in A 980's optical spectrum. These are the first-ever detections of germanium lines in an EHe's observed spectrum, and provide the first measurements of germanium abundance in an EHe star. The overabundance of germanium in A 980's atmosphere provides us with evidence for the synthesis of germanium in EHe stars. Among the known cool EHe stars, A 980 exhibits a maximum enhancement of the *s*-process elements based on significant number of transitions. The measured elemental abundances reveal signs of H-burning, He-burning, and specifically the nucleosyntheses of the key elements: Ge, Sr, Y, Zr, and Ba. The nucleosyntheses of these key elements are discussed in light of asymptotic giant branch evolution and the expectation from the accretion of an He white dwarf by a C-O white dwarf or by a neutron star.

Keywords: stars: Extreme Helium Stars (EHes) — stars: Chemical abundances — stars: Hydrogen-deficient Carbon Stars (HdCs) — stars: Chemically peculiar

1. INTRODUCTION

There exists a distinct category of hydrogen-deficient stars that have enhanced carbon features and diminished hydrogen Balmer lines, in their observed spectra, than expected for their effective temperatures. This was first pointed out by [Bidelman \(1953\)](#).

[Bidelman \(1953\)](#) has listed four stars in this category, and these are not light or photometric variables¹. [Warner \(1963\)](#) included one more star, HD 148839, in this category of non-variables. Note that the observed spectrum of HD 148839 shows the usual presence of enhanced C₂ bands and C I lines, and the absence of CH band, except for not very weakened Balmer lines.

Until the year 2022, there were just these five known in this category coined as hydrogen-deficient carbon (HdC) stars. Earlier, [Warner \(1967\)](#) conducted an abundance analysis of these five stars to investigate their surface composition. A recent survey has reported 27 new HdCs based on their low-resolution spectra - about a sixfold increase in their number than the earlier known ([Tisserand et al. 2022](#)). Detailed abundance analysis serves as a crucial observational constraint on theoretical models concerning the formation and evolution of these peculiar stars.

In this paper we conduct an abundance analysis of a new warm HdC, A 980 (2MASS 18113561+0154326), using a high-resolution spectrum.

2. OBSERVATIONS, DATA REDUCTION, AND LINE IDENTIFICATION

We have obtained a high-resolution optical spectrum of the newly identified warm HdC star A 980 using the Hanle Echelle Spectrograph (HESP) mounted on 2-m Himalayan Chandra Telescope (HCT) at the Indian Astronomical Observatory (IAO) in Hanle, Ladakh, India. These observations were made on 21 June 2023. The

Corresponding author: Ajay Kumar Saini
ajay.saini@iiap.res.in

¹ Notably, there exists yet another class of hydrogen-deficient stars known as R Coronae Borealis (RCB) stars. RCB stars exhibit remarkable photometric variability by undergoing unpredictable light decline (up to about 9 mag in visual) in a matter of few weeks and recover to their maximum light in about few to several months ([Clayton 1996](#)).

spectrum was recorded onto a $4k \times 4k$ CCD that covered the wavelength range from 3856 \AA to 9656 \AA with a resolving power ($R = \lambda/\Delta\lambda$) of about 30 000. A total of three frames, each of 45 minutes exposure, were observed and co-added to improve the signal-to-noise ratio (SNR) (ranging from 25 to 180 per pixel across the covered spectral range from blue to red). A Th-Ar hollow cathode lamp was observed for wavelength calibration. To normalize the pixel-to-pixel variation in the sensitivity of the CCD, several exposures known as flat frames with differing spectrograph focus (in focus and out of focus) were acquired using a featureless quartz-halogen lamp. All the flat frames were combined to create a master flat with a very high signal for flat correction. A telluric standard, that is a rapidly rotating B-type bright star, was also observed on the same night to get rid of Earth's atmospheric absorption lines. The observed spectrum of the star was then reduced utilizing the standard tasks under the Image Reduction and Analysis Facility (IRAF) software package (Tody 1986, 1993). In IRAF, the task `telluric` is used to remove Earth's atmospheric absorption lines by dividing the observed telluric standard spectrum from the observed spectrum of our program star.

For the spectral line identifications, we have used the NIST Atomic Spectra Database², A multiplet table of astrophysical interest - revised edition (Moore 1972), Tables of spectra of H, C, N, and O (Moore 1993), Kurucz's database³ and VALD database⁴. A large spectral coverage ($3856\text{-}9656 \text{ \AA}$) of the star's observed spectrum has enabled us to identify several important elements with their significant number of lines, of about 1900, and their ionization stages. The observed absorption line spectrum is well represented by neutral helium lines, neutral and singly ionized carbon lines, and also by plenty of singly ionized metal lines of the iron group⁵. Singly ionized helium is not detected in the spectrum. Lines of all elements expected and observed in early A-type and late B-type normal stars are found. The observed spectrum exhibits remarkably diminished hydrogen Balmer lines and the absence of C_2 molecular features. We note that the above described characteristics fit well with the observed absorption lines of an extreme helium (EHe) star especially, the cooler EHes (Pandey et al. 2001). A comparison with the available high-resolution spectrum of the cool EHe, LS IV -14° 109, reveals that the observed

spectrum of the program star A 980 is a near replica of the former except for the significantly enhanced absorptions of neutron-capture elements in A 980's spectrum (see Figure 1, top left panel, for example). The presence of He I line in the observed spectrum of A 980 is also shown along with that of LS IV -14° 109 in Figure 2d. The observed spectrum of an HdC, HD 173409 (available from Hema et al. (2012)) when compared with that of A 980 shows the absence of the C_2 molecular features in A 980 (see Figure 1, bottom left panel, for example). These comparisons clearly demonstrate that A 980 is not an HdC star. However, Tisserand et al. (2022) have classified A 980 as a warm HdC star, and have renamed the category of HdCs as dustless HdC (dlHdC) stars.

Among the several absorptions of the neutron capture elements in A 980's spectrum, the notable were the identifications of singly-ionized germanium Ge II lines.

2.1. Ge II lines

Only two multiplets are listed in the Revised Multiplet Table (RMT; Moore (1972)) for the identification of Ge II lines. Out of the two Ge II lines of RMT 1, the line at 6021.09\AA is clearly present in A 980's spectrum while the stronger line at 5893.42\AA is severely blended as engulfed by a strong ISM-NaD₁ component. No Ge II lines of RMT 2 are detected in the observed spectrum. However, the NIST Atomic Spectra Database provides more multiplets that include the above-discussed two multiplets listed in the RMT for further line identification. A thorough search was made for all Ge II lines of these multiplets. Two more unblended Ge II lines, $\lambda 7049.37$ and $\lambda 7145.39$, from multiplet $^2D - 2P^0$ of transition array $4s4p^2 - 4s^25p$ were identified; the third line $\lambda 6966.32$ of this multiplet is severely contaminated by a Fe II line. The Ge II line $\lambda 6021.09$ that was identified using the RMT is from multiplet $^2S - 2P^0$ of transition array $4s^25s - 4s^25p$. We note that Ge II lines from the multiplets of the excited levels with lower excitation potentials of 9.7 eV or higher have negligible contribution to the observed spectrum of A 980. We also searched for Ge II lines in the available spectra of three cooler EHes: LS IV -14° 109, FQ Aqr, and LSS 3378 (see Pandey et al. (2001); Pandey & Reddy (2006)). All the Ge II lines that were detected in A 980's spectrum are also present in the available spectrum of LS IV -14° 109. Along with these detected lines, the spectrum of LS IV -14° 109 revealed an additional unblended line $\lambda 5893.39$, the strongest line from the multiplet RMT 1, $^2S - 2P^0$, which was expected to be present in A 980's spectrum but was severely contaminated as discussed earlier. Our search for all the above identified Ge II lines, including the strongest line at 5893.39\AA , in the available spectra

² see <https://physics.nist.gov/asd>

³ see <http://kurucz.harvard.edu>

⁴ see <https://vald.astro.uu.se>

⁵ The radial velocity (R.V.) of A 980, determined from the identified Fe II lines, is measured to be $109 \pm 2 \text{ km s}^{-1}$.

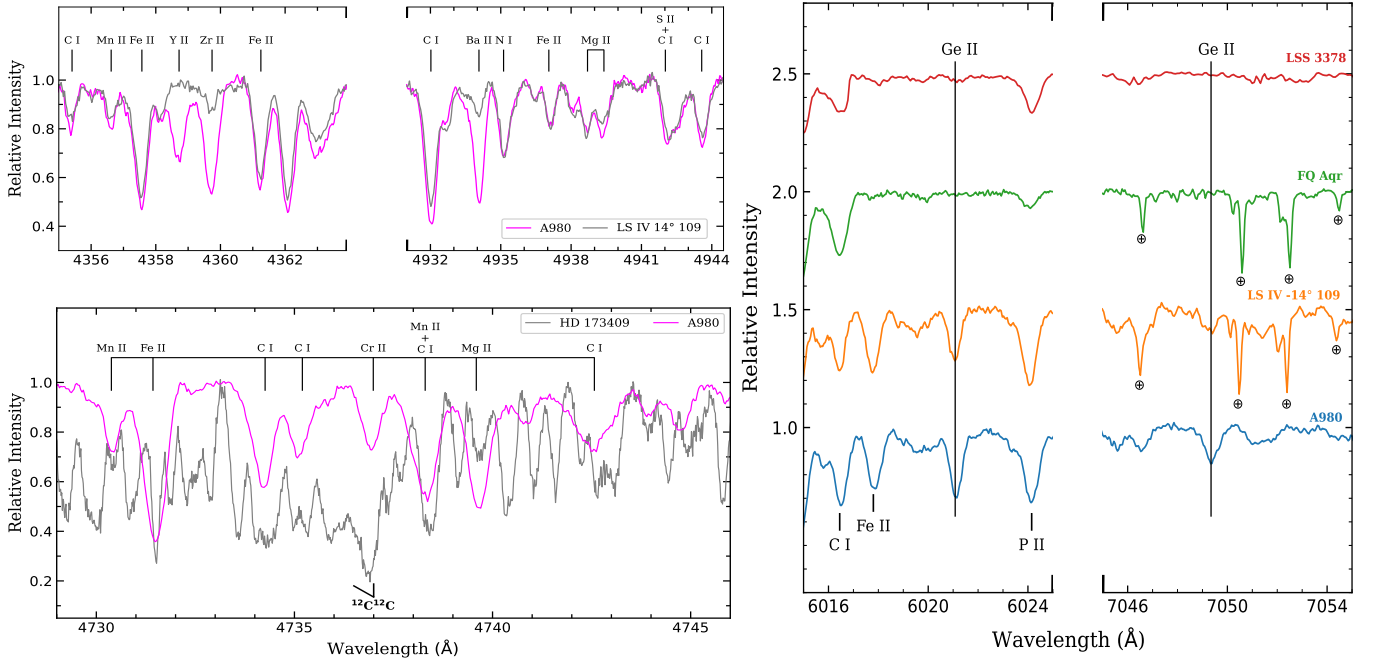


Figure 1. Observed spectra of LS IV -14° 109, a known cool EHe, and A 980 are shown for comparison (see top left panel). Observed spectra of HD 173409, a known HdC, and A 980 in (1, 0) C₂ band region for comparison (bottom left panel). In the right panel, identification of Ge II λ 6021.04 and 7049.37 Å lines in A 980 and other cool EHes LS IV -14° 109, FQ Aqr, and LSS 3378 are highlighted by vertical lines. The principal lines are marked. The telluric absorption lines are shown by encircled crosses. The key is provided on each panel.

of the other two cool EHes: FQ Aqr and LSS 3378 was unsuccessful (for example, see right panel of Figure 1).

3. ABUNDANCE ANALYSIS - PROCEDURE

The procedure for abundance analysis involves predicting the observed spectrum using a grid of model atmospheres combined with a radiative transfer code in local thermodynamic equilibrium (LTE). The predictions of an observed spectrum were made in the sense of computing the line equivalent width or synthesizing the line spectrum.

3.1. Hydrogen-deficient model atmospheres

For the analysis of A 980, a cool EHe star, the same procedure is followed as described in Pandey et al. (2001). The abundance analysis uses two grids of line-blanketed hydrogen-deficient model atmospheres; one with $T_{\text{eff}} \leq 9500$ K and the other with $T_{\text{eff}} \geq 10\,000$ K. The grid of $T_{\text{eff}} \leq 9500$ K, the Uppsala line-blanketed models, is described by Asplund et al. (1997), and that of $T_{\text{eff}} \geq 10\,000$ K was computed by the code STERNE (Jeffery & Heber 1992). The line formation calculations, which involve computing the line equivalent width as well as the spectrum synthesis using the Uppsala models, were carried out with the Uppsala LTE line-formation code EQWIDTH. Similarly, spectrum synthesis code SYNSPEC (Hubeny & Lanz 2017) was adopted

for the line formation calculations using STERNE as well as Uppsala models.

3.2. Consistency between line-formation codes, and between model grids

For an adopted model atmosphere, the abundances derived using SYNSPEC and EQWIDTH for weak lines are in good agreement within 0.1 dex for a majority of the species. We notice that the abundances derived using the former are always lower than those derived using the latter. We attribute these small differences to the adopted continuous opacity data being from two different sources.

The two model atmosphere grids, as discussed above, do not overlap in effective temperature. These two grids are compared by deriving a model for 9500 K using extrapolation of the high-temperature grid whose coolest models are at 10 000 K. The extrapolated model and an Uppsala model for 9500 K gave identical abundances to within 0.05 dex (Pandey et al. 2001).

3.3. Atomic data

The gf -values and excitation potentials for most of the lines used in our LTE analysis were available in the NIST database. The data for the remaining lines are from Kurucz database and other sources (see appendix: Table B2). However, for several Zr II lines, we have used new

improved experimental gf -values from the compilations of Ljung et al. (2006) and Malcheva et al. (2006). The Stark broadening and radiation broadening coefficients are mostly from the Kurucz database. The line broadening coefficients for computing the He I profiles are from Dimitrijevic & Sahal-Brechot (1984). The line broadening treatments for synthesizing hydrogen Balmer lines are from Hubeny et al. (1994) as used by SYNSPEC. See appendix: Table B2 for the detailed line list used in our analysis.

3.4. Atmospheric parameters and elemental abundances

A model atmosphere is characterized by its effective temperature, surface gravity, and chemical composition. The input elemental abundances of the adopted model atmosphere need to be consistent with those derived from the observed spectrum. A model atmosphere of an EHe star is mainly governed by the input carbon and helium abundances. Specifically, both carbon and helium are the major contributors to the continuum opacity in cool EHes (Pandey et al. 2001). Hence, the input C/He ratio of the adopted model atmosphere needs to be in accord with that determined from the star’s observed spectrum. The input composition of the rest of the elements is scaled to solar with H/He fixed at 10^{-4} by number.

A fine abundance analysis starts with deriving the star’s effective temperature (T_{eff}), surface gravity ($\log g$), and the microturbulent velocity (ξ). Subsequently, the photospheric elemental abundances are estimated for the adopted model atmosphere. These parameters are determined from the observed line spectrum.

The microturbulent velocity ξ (in km s^{-1}) is first determined by imposing that the lines of a particular species, neutral or ionized, with similar lower excitation potential (LEP) and having a range in their measured equivalent widths, return the same abundance.

Second, the condition of the ionization balance needs to be satisfied i.e., for an element represented in the observed spectrum by neutral as well as the ionized states must return the same abundance from lines of different stages of ionization. This designates a locus in the (T_{eff} , $\log g$) plane. Such elements with their pairs of ions provide loci of very similar slope in the (T_{eff} , $\log g$) plane.

The third condition that needs to be satisfied is the excitation balance which serves as a thermometer measuring T_{eff} . This requires that the lines of a particular species but of differing LEPs should return the same elemental abundance. The model grid is searched for the model that meets this condition. The optimum T_{eff} is found to be independent of the adopted $\log g$ and C/He

for the model atmosphere. Hence, this indicator provides a locus in the (T_{eff} , $\log g$) plane to lift the degeneracy presented by the ionization balance. A second indicator may be available: for stars hotter than about 10000 K, the He I profiles are less sensitive to T_{eff} than to $\log g$ on account of pressure broadening due to the quadratic Stark effect.

In reproducing the observed spectrum by spectrum synthesis, we include broadening due to the instrumental line profiles, the microturbulent velocity ξ and assign all additional broadening, if any, to rotational broadening. Observed unblended line profiles, preferably weak, are used to obtain the additional broadening. Synthetic line profile, including the broadening due to instrumental profile, for the adopted model atmosphere (T_{eff} , $\log g$, ξ) and the abundance (from equivalent width analysis), is found to be sharper than the observed line profiles. This extra broadening in the observed profile is attributed to rotational broadening.

4. A 980 – ABUNDANCE ANALYSIS RESULTS

A test model atmosphere is adopted with ($T_{\text{eff}} = 9500$ K, $\log g = 1.0$, C/He = 1%) to first determine the microturbulent velocity ξ . These stellar parameters were chosen due to the near identical observed spectra of A 980 and LS IV -14° 109 (see Section 2). The stellar parameters derived for LS IV -14° 109 by Pandey et al. (2001) are the same as adopted above. ξ is determined from lines of Fe II, Ti II, Cr II, and C I. ξ is found to be 11.0 km s^{-1} from Fe II and Ti II lines while that from Cr II and C I lines is 12.0 km s^{-1} and 11.5 km s^{-1} , respectively. We finally adopt a mean ξ of $11.5 \pm 1.0 \text{ km s}^{-1}$ for determining the elemental abundances. For example, see Figure 2a that illustrates the procedure of estimating ξ .

T_{eff} was obtained from Fe II lines that exhibit a range in their lower excitation potentials (LEP): 2 to 11 eV. For $\xi = 11.5 \text{ km s}^{-1}$, we found a model (T_{eff} , $\log g$, ξ) that provided the same abundance independent of the line’s LEP. The T_{eff} deduced from the Fe II lines has negligible dependence on the adopted model’s $\log g$ and C/He ratio. Figure 2b illustrates the procedure for obtaining T_{eff} . The loci obtained from Fe II/Fe I, N II/N I, Si II/Si I, and S II/S I ionization balance are shown in Figure 2c. These combined with the T_{eff} deduced from the excitation balance of Fe II lines, that has negligible dependence on surface gravity, eventually provide the optimum stellar parameters: $T_{\text{eff}} = 9250 \pm 250$ K, $\log g = 1.2 \pm 0.3 \text{ cm s}^{-2}$ (cgs), and $\xi = 11.5 \pm 1.0 \text{ km s}^{-1}$.

For the derived stellar parameters, the C/He ratio may directly be determined from the measured equivalent widths of C I and C II lines. The observed He I line profiles are presumably yet another indicator of the

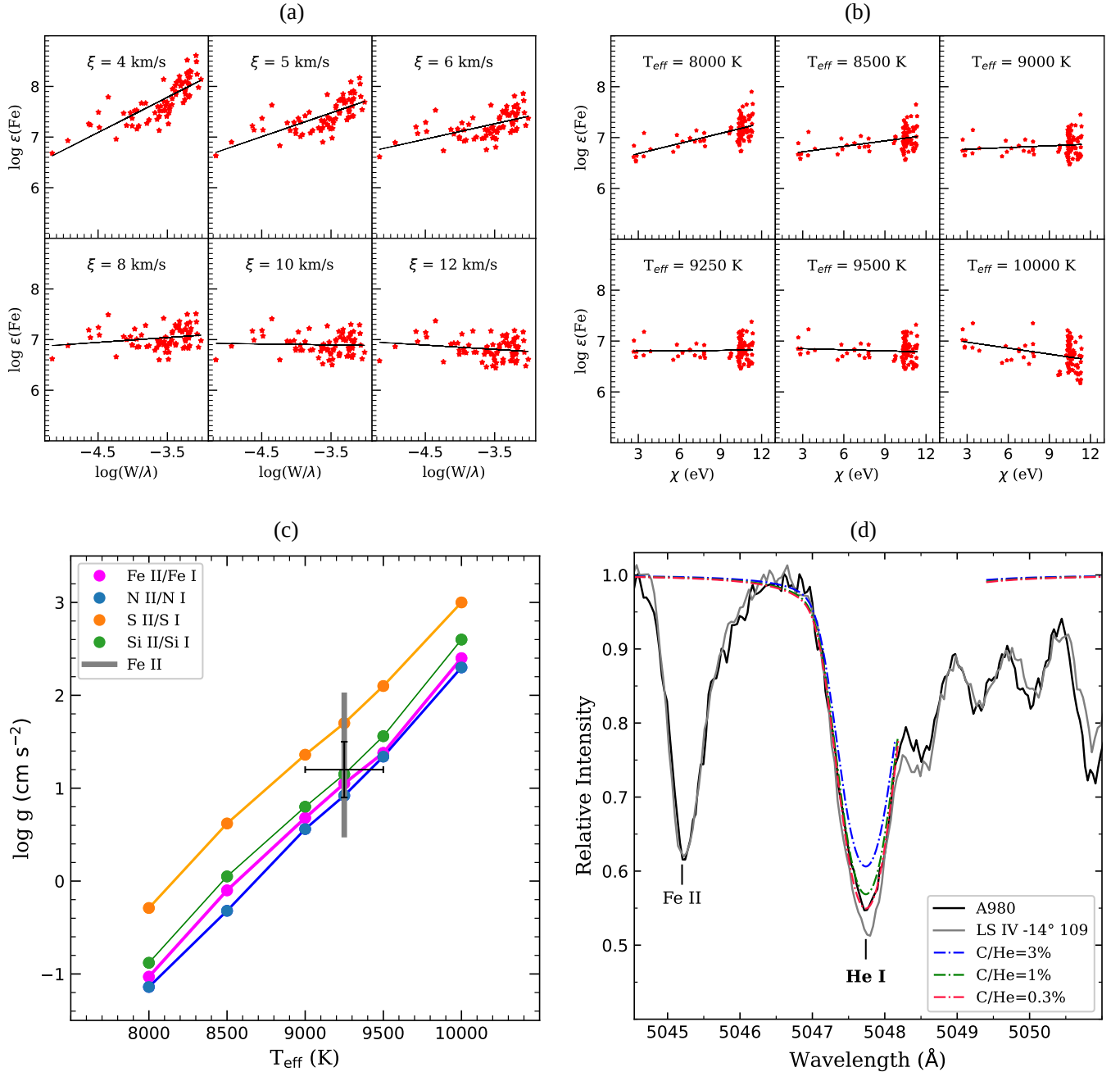


Figure 2. (a) Abundances from Fe II lines for A 980 versus their reduced equivalent widths ($\log W_{\lambda}/\lambda$). A value of $\xi = 11.0$ km/s is obtained from this figure. (b) Abundances from Fe II lines for A 980 versus their lower excitation potential (χ), showing excitation equilibrium. A value of $T_{\text{eff}} = 9250 \pm 250$ K is obtained from this figure. (c) The (T_{eff} , $\log g$) plane of A 980 shows the final values of T_{eff} and $\log g$ with error bars. Loci satisfying ionization equilibria are plotted – see keys on the figure. The excitation equilibrium of Fe II lines is shown by thick & solid gray line. (d) Synthesized and observed He I $\lambda 5047.74$ Å profiles. The He I line profiles are synthesized using the model $T_{\text{eff}} = 9250$ K, $\log g = 1.25$ cgs and $\xi = 11.5$ km s $^{-1}$ for three different values of C/He values. The observed He I $\lambda 5047.74$ Å profile of LS IV -14° 109 is also shown for comparison. The key is provided on each panel.

C/He ratio. Figure 5 of Pandey et al. (2001) illustrates the predicted equivalent widths of C I, C II, and He I lines for a model's C/He ratio. At the derived T_{eff} and $\log g$

of A 980, the predicted C I line strengths are insensitive to the model's C/He $\geq 1.0\%$; C/He of 1% corresponds to carbon abundance, $\log \epsilon(\text{C}) = 9.5$. However, the C II

line strengths are nearly insensitive to the model’s C/He $\geq 0.3\%$. The observed C II lines are very strong and the measured equivalent widths are very large. Hence, we conclude that C II lines are not fit for estimating the C/He ratio and instead use C I lines for determining the same.

The C I lines return carbon abundances of $\log \epsilon(\text{C}) = 8.9 \pm 0.2$, 9.0 ± 0.2 , and 9.3 ± 0.2 for the optimum model’s input ratio of C/He = 0.3% ($\log \epsilon(\text{C}) = 9.0$), 1.0% ($\log \epsilon(\text{C}) = 9.5$), and 3.0% ($\log \epsilon(\text{C}) = 10.0$), respectively. We find that the input model’s carbon abundance is consistent with that derived for the optimum model with a C/He of 0.3%. He I profiles at 5048, 5876, and 6678 Å may provide an estimate of the C/He ratio. The best fitting observed profile of He I is shown in Figure 2d. A ratio C/He of about 0.3% produces an acceptable fit to the He I profile. Within the uncertainties, mainly line-to-line scatter, a ratio C/He = 0.3% is determined from the C I lines as well as the He I profiles independently.

The final abundances, as given in Table 1, are derived for the optimum model of C/He = 0.3%. The derived abundances are normalized based on the convention that $\log \epsilon(\text{X}) = \log(\text{X}/\text{H}) + 12.0$ to a scale in which $\log \sum \mu_I \epsilon(I) = 12.15$, where 12.15 is determined from solar abundances with He/H $\simeq 0.1$. Here, μ_X is the atomic weight of element X. Since all elements but He have a very low abundance, the helium abundance $\log \epsilon(\text{He})$ is 11.54 on this scale. The hydrogen abundance is from the syntheses of H α , H β , and H γ profiles, for example, see appendix: Figure C1. Neutral lines of the key element fluorine are also present in the spectrum of A 980 like other cool EHes (Pandey 2006). Fluorine abundance is determined by spectrum syntheses of neutral fluorine (F I) lines (see Figure 3, bottom panels). The abundance of germanium, a very significant element for this study, is from spectrum syntheses of Ge II lines at 6021.04, 7049.37, and 7145.39Å (see Figure 3, top panels). The deduced projected rotational velocity ($v \sin i$) of about 15 km s $^{-1}$ is adopted for spectrum syntheses.

5. SURFACE COMPOSITION – DISCUSSION

The derived surface composition of A 980 is summarized in Table 1 along with the comparison star LS IV -14° 109 (Pandey et al. 2001); also given are the solar abundances from Asplund et al. (2009). The derived abundances of the cool EHe A 980 are then compared with the measured abundances of other EHes from the literature (see Pandey et al. (2021) and references therein).

The surface composition of A 980 clearly reveals that its atmosphere is hydrogen poor and rich in helium and

Table 1. Derived elemental abundances for A 980 and LS IV -14° 109.

Element	A 980 ^b		LS IV -14° 109 ^c		
	Solar ^a	$\log \epsilon(\text{X})$	$[\text{X}/\text{Fe}]$	$\log \epsilon(\text{X})$	$[\text{X}/\text{Fe}]$
H	12	5.81	-5.39	6.20	-5.30
He	10.93	11.54	1.41	11.54	1.11
C	8.43	8.87	1.24	9.45	1.52
N	7.83	8.40	1.37	8.60	1.27
O	8.69	7.89	0.00	8.50	0.31
F	4.56	6.10	2.34	6.52	2.46
Ne	7.93	8.65	1.52	9.40	1.97
Na	6.24	6.46	1.02	6.80	1.06
Mg	7.60	7.00	0.20	7.20	0.10
Al	6.45	6.14	0.49	6.90	0.95
Si	7.51	7.30	0.59	7.68	0.67
P	5.41	5.36	0.75	5.30	0.39
S	7.12	6.89	0.57	7.55	0.93
Ar	6.40	5.99	0.39
Ca	6.34	5.64	0.10	5.55	-0.29
Sc	3.15	2.98	0.63	3.30	0.65
Ti	4.95	4.27	0.12	4.30	-0.15
V	3.93	3.40	0.27
Cr	5.64	4.75	-0.09	5.10	-0.04
Mn	5.43	4.85	0.22	5.30	0.37
Fe	7.50	6.70	0.00	7.00	0.00
Co	4.99	4.72	0.53
Ni	6.22	5.50	0.08	5.92 ^d	0.20
Ge	3.65	3.72	0.87	3.48 ^b	0.33
Sr	2.87	3.40	1.33	2.60	0.23
Y	2.21	2.54	1.13	1.90	0.19
Zr	2.58	2.93	1.15	1.90	-0.18
Ba	2.18	2.23	0.85	1.70	0.02

^aSolar abundances are adopted from Asplund et al. (2009)

^bThis work

^cAdopted from Pandey et al. (2001) and Pandey (2006)

^dFrom the unblended cleaner lines and their adopted *gf*-values used in this work for A 980

NOTE— $[\text{X}/\text{Fe}] = (\text{X}/\text{Fe})_{\star} - (\text{X}/\text{Fe})_{\odot}$

carbon as observed for most of the EHes. These are clues that the atmosphere of A 980 is contaminated by the products of H- and He- burning reactions. For the evolved low- and intermediate-mass stars, abundances of elements that are unlikely to be affected by H- and He-burning and attendant nuclear reactions are good indicators of their initial metallicity. These are

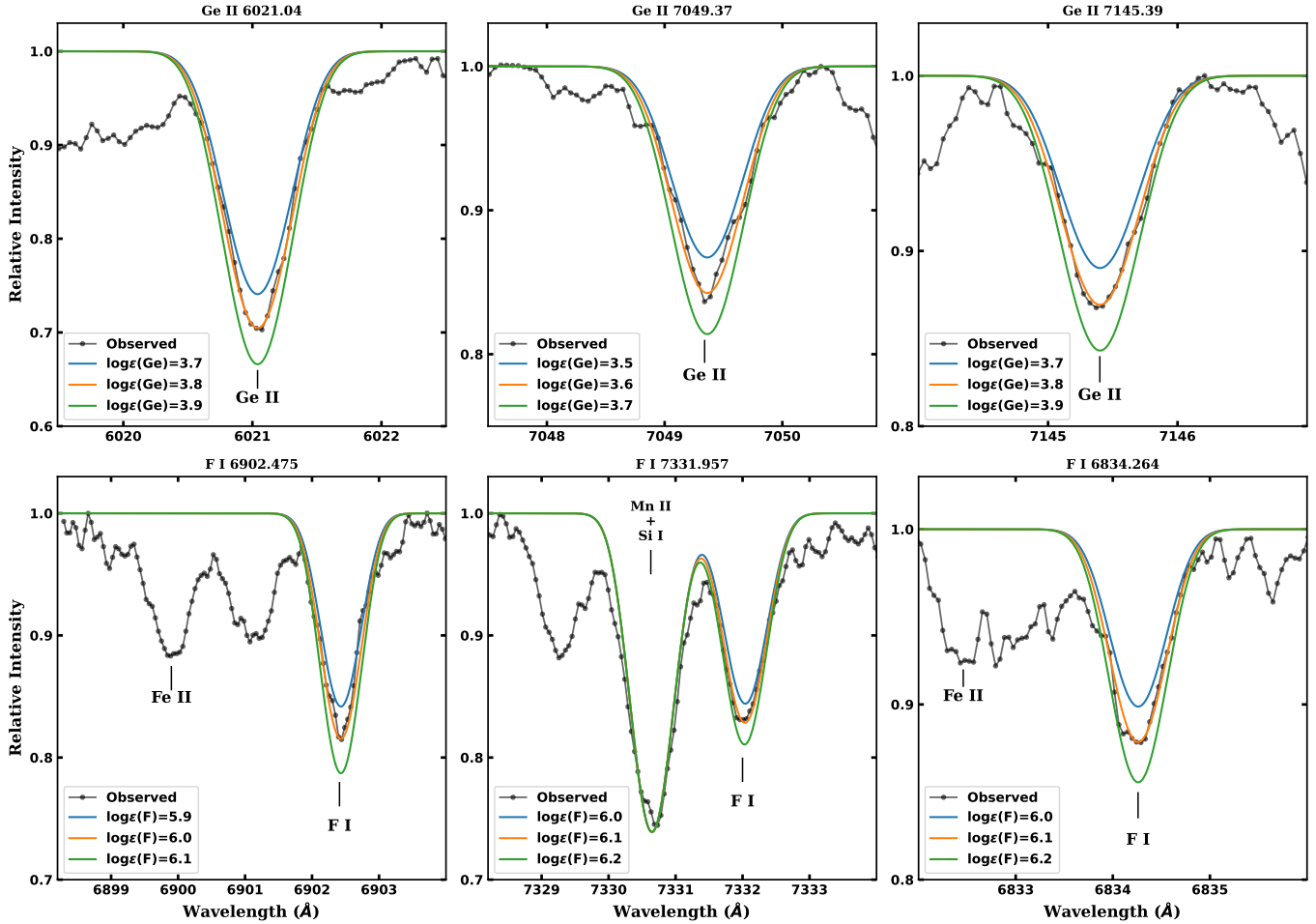


Figure 3. For A 980, top and bottom panels show the spectrum syntheses of Ge II and F I lines, respectively. See key on the Figures.

V, Cr, Mn, Fe, Co, and Ni – the iron-peak elements, and Mg, Si, S, Ca, Sc, and Ti – the α -elements. We note that A 980’s abundance ratios, Mg/Fe, Si/Fe, S/Fe, Ca/Fe, Sc/Fe, V/Fe, Cr/Fe, Mn/Fe, Co/Fe and Ni/Fe, are on average as expected for that in metal-poor normal and unevolved stars (see Table 1; Goswami & Prantzos (2000); Ryde & Lambert (2004)). We adopt iron abundance as the indicator of initial metallicity in A 980.

The abundances of elements that are affected in the course of A 980’s evolution are H, He, C, N, O, F, Ne, Ge, Sr, Yr, Zr, and Ba when compared to a normal star, for example, the Sun – see Table 1.

We discuss by comparing the derived surface composition of A 980 with other EHes. The surface composition of other EHes including the hot RCB star DY Cen are from Jeffery & Heber (1992); Drilling et al. (1998); Jeffery (1998); Jeffery et al. (1998); Pandey et al. (2001, 2004, 2006); Pandey (2006); Pandey & Reddy (2006); Pandey & Lambert (2011); Pandey et al. (2014);

Pandey & Lambert (2017); Jeffery (2017); Bhowmick et al. (2020); Jeffery et al. (2024).

Hydrogen – The hydrogen abundance $\log \epsilon(\text{H})$ is found to be 5.8 ± 0.2 which is under-abundant by a factor of $\sim 10^6$ relative to a normal star. A 980’s hydrogen abundance fits well within the range of 5–8 that is derived for other EHes (see Pandey et al. (2021) and references therein). The exceptions are the hot RCB, DY Cen, and the EHes with a very low carbon abundance (see the following section).

Carbon – The carbon abundance $\log \epsilon(\text{C})$ is found to be 8.9 ± 0.2 that is a C/He ratio of 0.0023. A 980 falls at the lower end of the range in the C/He ratios for other EHes. Here we exclude the four known EHes with a very low carbon abundance. However, recent studies suggest that HD 144941, one of these four, is the most extreme helium-strong star with extremely strong magnetic field (see Przybilla et al. (2021); Shultz et al. (2021)).

Nitrogen – Nitrogen abundance is enriched by a factor of 25 (1.4 dex) relative to the expected initial abun-

dance for A 980’s metallicity that is the Fe abundance. The enhanced nitrogen abundance shows the complete conversion of initial C, N, and O to N. This provides evidence for the operation of severe CNO cycling in an H-rich region.

Oxygen – Oxygen abundance is close to the initial value expected for A 980’s Fe abundance. The O/N ratio is found to be 0.94 for A 980 and is in concert with the other EHes having an O abundance close to their initial value (see Pandey et al. (2006)).

Fluorine – Fluorine abundance is significantly enhanced that is about a factor of 200 when compared with the F expected for A 980’s metallicity. This enhancement is in concert with other cool and hot EHes including the RCB stars (see Bhowmick et al. (2020)).

Neon – Neon abundances are from Ne I lines, and are subject to non-LTE effects. Application of the non-LTE effects most likely brings the Ne abundances of the cool EHes, here A 980, (down by about 0.8 dex) in line with the hot EHes (Pandey & Lambert 2011).

Germanium – The germanium abundance $\log \epsilon(\text{Ge})$, derived from spectrum synthesis, is 3.7 ± 0.1 . Relative to iron, Ge is overabundant with respect to solar by about a factor of 8 (0.9 dex). This provides the first measurement of germanium abundance in EHe stars.

Strontium, Yr, Zr, and Ba – Relative to iron, the abundances of Sr, Yr, Zr, and Ba are found to be overabundant with respect to solar by about a factor of 20 (1.3 dex), 13 (1.1 dex), 16 (1.2 dex) and 8 (0.9 dex), respectively. A 980 provides a maximum enhancement of *s*-process elements measured in a cool EHe star to date using significantly reliable number of transitions – these are 4, 12, 16, and 4 for Sr, Yr, Zr, and Ba, respectively.

6. DISCUSSION AND CONCLUSIONS

A fine abundance analysis based on A 980’s observed high-resolution spectrum clearly demonstrates that it is a cool EHe star.

The surface abundances of A 980 are measured especially for the key elements: CNO, fluorine, and the heavier elements: Ge, Sr, Y, Zr, and Ba. The measured C/He ratio is about 0.2% and has the lowest known C/He ratio. Note that the other EHes, excluding the four known EHes with a very low carbon abundance, exhibit a range in their C/He ratios: 0.3% – 1.3%.

EHe stars are thought to be products of double white dwarf mergers. Case1 Predictions from Figure 5 of Menon et al. (2019) for CO+He white dwarf mergers are in broad agreement with the observed abundances of A 980, in particular, the enhanced fluorine and the *s*-process elements (Y, Zr, Ba), compared to solar.

A significant addition is the determination of germanium abundance in two cool EHes, A 980 and LS IV -14° 109, with similar stellar parameters (T_{eff} , $\log g$). These are the first determination of Ge abundances in EHe stars. The atmosphere of A 980 is significantly enhanced in germanium that is, eight times higher than the solar value relative to iron. This notable enhancement is evidence of the synthesis of germanium in a cool EHe star, A 980. Note that A 980 is enriched by about a factor of 4 in germanium (Ge/Fe) relative to LS IV -14° 109 while A 980’s enrichment in germanium is about a factor of 16 when compared with a normal subgiant HD 107113 of similar metallicity; HD 107113’s Ge and Fe abundances are from Roederer (2012).

Two primary processes that could account for the synthesis of germanium are first the neutron-capture process (Karakas et al. (2007) and references therein) and second the rapid proton-capture process, known as the rp-process (Biehle 1994). Knowledge of the germanium production mechanism in A 980 will provide new clues to the origin of EHe stars. To identify the process of germanium production, A 980’s observed abundances: Ge, light *s*-process (Sr, Y, Zr), and heavy *s*-process (Ba), were compared with Karakas et al. (2018) predictions for low- to intermediate-mass asymptotic giant branch (AGB) stars (see Table 2). A 980’s mass is estimated to be $1 \pm 0.5 M_{\odot}$ based on its luminosity, that is calculated using the absolute magnitude from Tisserand et al. (2022), along with our derived surface gravity (g) and effective temperature (T_{eff}). For AGB stars, as given in Table 2, the abundance ratios are shaped by *s*-process nucleosynthesis. The expected ratios for low-mass AGB star ($2.5 M_{\odot}$) are $[\text{Ge}/\text{Fe}] = +0.5$, $[\text{Ge}/\text{ls}] = -1.1$, and $[\text{ls}/\text{hs}] = -0.7$. However, for A 980, the observed ratios are notably different: $[\text{Ge}/\text{Fe}] = +0.87$, $[\text{Ge}/\text{ls}] = -0.34$, and $[\text{ls}/\text{hs}] = +0.36$. Here, ls and hs represent the light and heavy *s*-process abundances, respectively. Specifically, the ratio $[\text{ls}/\text{hs}] > 0$ in A 980 contradicts low-mass AGB predictions where heavy *s*-process elements are expected to be more abundant. The expected ratios for intermediate-mass AGB star ($5 M_{\odot}$), with different mass loss rates: VW93 and B95, are provided in Table 2 (see Karakas et al. (2018) for VW93 and B95). Here, the ratio $[\text{ls}/\text{hs}] > 0$ for both cases and is in line with that observed for A 980. The abundance ratios for a mass loss rate, VW93, are found to be in fair agreement with that observed for A 980. This suggests that the atmospheres of A 980 are contaminated by germanium produced via the *s*-process taking place in an intermediate-mass AGB star. Note that the abundance ratios depend on the adopted mass loss rate for

Table 2. Surface abundance ratios for comparative analysis.

	A 980 ^a	CO+He ^b	AGB ^c		
			2.5M _⊙	5M _⊙ (VW93)	5M _⊙ (B95)
[Fe]	-0.80	-1.55	-0.70	-0.70	-0.70
[Ge/Fe]	+0.87	...	+0.50	+0.90	+0.30
[Ge/ls]	-0.34	...	-1.10	-0.10	+0.10
[Ge/hs]	+0.02	...	-1.80	+0.50	+0.25
[ls/hs]	+0.36	+0.50	-0.70	+0.60	+0.15
[Sr/Fe]	+1.33	...	+1.50	+1.10	+0.25
[Y/Fe]	+1.13	+1.35	+1.60	+1.05	+0.20
[Zr/Fe]	+1.15	+0.95	+1.70	+0.95	+0.15
[Ba/Fe]	+0.85	+0.65	+2.30	+0.40	+0.05

^aThis work^bAdopted from Menon et al. (2019): Case1 Predictions^cAdopted from Karakas et al. (2018)

intermediate-mass AGB stars but nucleosynthesis processes remain the same.

In comparison, the observed abundance ratios do suggest that the atmospheres of LS IV -14° 109 are not contaminated by freshly synthesized Ge and *s*-process elements (see Table 1).

Alternatively, a significant enhancement in germanium abundance is evident from Thorne-Żytkow Objects (TŻOs) and presumably produce elements via the rapid proton-capture process (rp-process). TŻOs are proposed as the possible merged products of a neutron star (NS) and a non-degenerate star. Farmer et al. (2023) provides the recent predictions of surface abundance ratios for Thorne-Żytkow Objects (TŻOs) but those are not in the regime of A 980's metallicity and the helium fraction to perform a comparative analysis.

The abundance ratios [ls/Fe] and [hs/Fe] for A 980 are similar to the predictions of CO+He WD mergers (Menon et al. 2019). However, predictions of germanium abundances are not available for CO+He white dwarf mergers to explore the origin of germanium in EHe stars. Theoretical studies for germanium synthesis in CO+He white dwarf mergers need to be explored.

7. ACKNOWLEDGMENTS

We thank the referee for a constructive review. This research was supported by the Science and Engineering Research Board (SERB), DST, India through grant: CRG/2021/000108. Ajay expresses gratitude to Sriram Krishna for his assistance with installing and running SYNSPEC. He also thanks Fayaz S. and B.P. Hema for

helping with the installation of the radiative transfer code EQWIDTH.

We thank the staff of IAO, Hanle, CREST, and Hosakote, who made these observations possible. The facilities at IAO and CREST are operated by the Indian Institute of Astrophysics, Bangalore.

APPENDIX

A. ERROR ANALYSIS

The adopted stellar parameters are accurate to typically: $\Delta T_{\text{eff}} = \pm 250$ K, $\Delta \log g = \pm 0.3$ cm s⁻², $\Delta \xi = \pm 1.0$ km s⁻¹. The line-to-line scatter, standard deviation due to the same ion holding many lines, and the uncertainty in stellar parameters are the major sources of errors in deriving abundances. The abundance errors due to line-to-line scatter are given in Table B2 while errors due to uncertainty in the stellar parameter are given in Table A1. Typically, the error due to uncertainty in the stellar parameter was found to be lesser than the line-to-line scatter. The abundance derived from more lines is always better and more reliable than those derived from fewer lines. However, this has a negligible effect on the mean abundance of element E. Therefore, we also include a weight due to the number of lines that derive the ion's abundance. The mean abundance of an element E was calculated as -

$$\langle E \rangle = \frac{\langle E_a \rangle + \langle E_b \rangle}{2}$$

where $\langle E_a \rangle$ and $\langle E_b \rangle$ are mean abundances of an element E, calculated by giving weight due to line-to-line scatter and number of lines respectively. They are defined as -

$$\langle E_a \rangle = \frac{w_{1a} \langle EI \rangle + w_{2a} \langle EII \rangle + \dots}{w_{1a} + w_{2a}}$$

where $\langle EI \rangle, \langle EII \rangle, \dots$ are the abundances derived from neutrally-ionized, singly-ionized, ... lines of element E. w_{1a}, w_{2a}, \dots are weights due to line-to-line scatter of ions ($\delta(EI), \delta(EII), \dots$), i.e.,

$$w_1 = \frac{1}{(\delta(EI))^2}$$

And,

$$\langle E_b \rangle = \frac{w_{1b} \langle EI \rangle + w_{2b} \langle EII \rangle + \dots}{w_{1b} + w_{2b}}$$

where w_{1b}, w_{2b}, \dots are weights due to the number of lines used to derive the abundance of ions, i.e.,

$$w_{1b} = \# \text{ of lines used to derive } \langle EI \rangle$$

Table A1. Errors in elemental abundances due to uncertainties in the stellar parameters. The abundance error due to ΔT_{eff} is the difference in abundances derived from the adopted model ($T_{\text{eff}}, \log g, \xi$) and a model ($T_{\text{eff}} + \Delta T_{\text{eff}}, \log g, \xi$). The abundance error due to $\Delta \log g$ is the difference in abundances derived from the adopted model ($T_{\text{eff}}, \log g, \xi$) and a model ($T_{\text{eff}}, \log g + \Delta \log g, \xi$). The abundance error due to $\Delta \xi$ is the difference in the abundances derived from the adopted model ($T_{\text{eff}}, \log g, \xi$) and a model ($T_{\text{eff}}, \log g, \xi + \Delta \xi$).

Species	$\Delta T_{\text{eff}} = +250$	$\Delta \log g = +0.25$	$\Delta \xi = +1.0$	rms
	(K)	(cgs)	(km s ⁻¹)	
C I	+0.12	-0.06	-0.03	0.13
C II	-0.17	+0.08	-0.15	0.24
N I	+0.08	-0.03	-0.02	0.09
N II	-0.12	+0.06	-0.03	0.14
O I	+0.06	-0.02	-0.05	0.08
Ne I	-0.16	+0.10	-0.09	0.21
Na I	+0.12	-0.06	-0.04	0.14
Mg I	+0.23	-0.10	-0.03	0.25
Mg II	+0.03	0.00	-0.01	0.03
Al II	-0.10	+0.07	-0.08	0.15
Si I	+0.15	-0.06	0.00	0.16
Si II	-0.08	+0.06	-0.05	0.11
P II	-0.09	+0.09	-0.03	0.13
S I	+0.13	-0.06	-0.01	0.14
S II	-0.09	+0.07	-0.05	0.13
Ca II	+0.14	-0.05	-0.02	0.15
Sc II	+0.23	-0.03	-0.01	0.23
Ti II	+0.17	-0.01	-0.04	0.17
V II	+0.14	+0.02	-0.02	0.14
Cr II	+0.08	+0.03	-0.04	0.09
Mn II	+0.06	+0.04	-0.02	0.07
Fe I	+0.21	-0.08	-0.01	0.22
Fe II	-0.01	+0.04	-0.03	0.05
Co II	+0.04	+0.05	-0.03	0.07
Ni I	+0.17	-0.07	0.00	0.18
Ni II	0.00	+0.05	-0.03	0.06
Ge II	+0.05	+0.12	+0.04	0.14
Sr II	+0.25	-0.05	-0.18	0.30
Y II	+0.26	-0.04	-0.03	0.27
Zr II	+0.21	-0.02	-0.03	0.22

Table A1 continued

Table A1 (continued)

Species	$\Delta T_{\text{eff}} = +250$	$\Delta \log g = +0.25$	$\Delta \xi = +1.0$	rms
	(K)	(cgs)	(km s^{-1})	
Ba II	+0.26	-0.06	-0.05	0.27

B. LINES USED FOR ABUNDANCE ANALYSIS

The lines used for the abundance analysis of A980 are given in Table B2. Also, the lower excitation potential (χ), $\log gf$, equivalent width (W_λ), and abundance ($\log \epsilon$) derived for each line are listed. The elemental abundances are derived by using model atmospheres with $T_{\text{eff}} = 9250$ K, $\log g = 1.25$ cm s^{-2} , C/He = 0.3% and microturbulent velocity $\xi = 11.5$ km s^{-1} .

Table B2. Lines used to derive elemental abundances for A980.

Ion		W_λ			
λ (\AA)	χ (eV)	$\log gf$	(m\AA)	$\log \epsilon^a$	Reference ^b
H I					
6562.82	10.20	0.710	Synth	5.62	NIST
4861.33	10.20	-0.020	Synth	5.80	NIST
4340.47	10.20	-0.447	Synth	6.00	NIST
Mean:				5.81 ± 0.16	
He I					
5048.00	21.22	-1.587	Synth	11.54	NIST
C I					
6595.24	8.85	-2.400	104	8.84	NIST
6591.45	8.85	-2.400	101	8.82	NIST
6683.95	8.85	-2.230	216	9.16	NIST
6688.79	8.85	-2.130	188	8.95	NIST
6711.29	8.86	-2.690	95	9.09	NIST
7022.24	8.64	-2.670	114	9.05	NIST
7074.86	8.64	-2.120	159	8.71	NIST
7132.11	8.65	-2.200	127	8.66	NIST
7473.31	8.77	-2.040	200	8.89	NIST
7837.11	8.85	-1.780	193	8.63	NIST
7840.27	8.85	-1.840	191	8.68	NIST
7852.86	8.85	-1.680	205	8.58	NIST
8018.56	8.85	-2.100	113	8.58	NIST

Table B2 continued

Table B2 (continued)

Ion		W_λ			
λ (\AA)	χ (eV)	$\log gf$	(m\AA)	$\log \epsilon^a$	Reference ^b
8078.48	8.85	-1.820	208	8.70	NIST
5824.64	8.85	-2.600	127	9.13	NIST
6012.24	8.64	-2.000	220	8.79	NIST
6078.40	8.85	-2.300	167	9.01	NIST
6108.53	8.85	-2.500	113	8.96	NIST
5540.76	8.64	-2.400	200	9.12	NIST
5547.27	8.64	-2.300	201	9.02	NIST
4817.37	7.48	-3.040	210	9.16	NIST
4943.58	8.65	-2.460	159	9.03	NIST
5159.92	8.64	-2.150	175	8.77	NIST
4355.41	7.68	-3.330	80	9.01	NIST
6671.84	8.85	-1.650	273	8.79	NIST
7087.83	8.65	-1.440	279	8.48	NIST
7093.25	8.65	-1.700	270	8.72	NIST
7685.17	8.77	-1.520	294	8.70	NIST
7832.63	8.85	-1.810	277	8.97	NIST
8014.98	8.85	-1.600	280	8.75	NIST
8062.36	8.85	-1.860	255	8.91	NIST
8070.42	8.85	-1.950	266	9.04	NIST
8083.80	8.85	-1.730	248	8.75	NIST
5793.12	7.95	-2.060	295	8.71	NIST
6001.13	8.64	-2.100	297	9.17	NIST
6007.18	8.64	-2.100	224	8.91	NIST
6010.68	8.64	-1.900	257	8.83	NIST
6016.45	8.64	-1.800	245	8.68	NIST
5551.03	8.65	-1.600	280	8.61	NIST
5548.90	8.65	-1.760	271	8.74	KP
4734.26	7.95	-2.370	279	9.02	NIST
4766.67	7.48	-2.620	255	8.91	NIST
7202.26	9.00	-1.900	199	8.87	NIST
7216.03	9.17	-2.300	139	9.12	NIST
7364.73	9.00	-1.840	216	8.88	NIST
7987.89	9.17	-2.100	169	9.03	NIST
Mean:				8.87 ± 0.18	
C II					
6578.05	14.45	-0.022	610	9.61	NIST
6582.88	14.45	-0.323	515	9.46	NIST
7231.32	16.33	0.038	360	9.51	NIST

Table B2 continued

Table B2 (continued)

Ion		W_λ			
λ (Å)	χ (eV)	$\log gf$	(mÅ)	$\log \epsilon^a$	Reference ^b
Mean:		9.53 ± 0.07			
N I					
6622.53	11.76	-1.504	215	8.53	NIST
6644.96	11.76	-0.858	270	8.09	NIST
6653.41	11.76	-1.138	220	8.19	NIST
6637.01	11.75	-1.432	186	8.34	NIST
6646.52	11.75	-1.539	134	8.22	NIST
6708.76	11.84	-1.288	210	8.35	NIST
6926.67	11.84	-1.475	131	8.20	NIST
6945.18	11.84	-1.100	241	8.30	NIST
6951.60	11.84	-1.525	204	8.57	NIST
6979.19	11.84	-1.542	118	8.20	NIST
6982.03	11.84	-1.525	174	8.45	NIST
7485.18	12.01	-1.572	135	8.44	NIST
7546.21	12.00	-1.313	150	8.24	NIST
7550.91	12.01	-1.213	172	8.25	NIST
5616.56	11.76	-1.370	246	8.48	KP
5600.53	11.76	-2.020	118	8.58	KP
5816.49	11.79	-2.070	108	8.60	NBS
5856.00	11.79	-2.110	80	8.47	NBS
6008.47	11.60	-1.406	215	8.31	NIST
5378.27	10.93	-2.841	50	8.50	NIST
5557.38	11.75	-1.735	83	8.09	NIST
5560.34	11.75	-1.181	192	8.07	NIST
4935.12	10.69	-1.891	165	8.09	NIST
4963.99	11.76	-2.140	111	8.67	KP
6471.03	11.75	-1.890	80	8.26	KP
Mean:		8.34 ± 0.18			
N II					
4643.08	18.48	-0.371	63	8.34	NIST
4607.16	18.46	-0.522	55	8.38	NIST
5679.56	18.48	0.225	130	8.63	NIST
5686.21	18.47	-0.586	65	8.78	NIST
Mean:		8.53 ± 0.21			

Table B2 continued

Table B2 (continued)

Ion		W_λ			
λ (Å)	χ (eV)	$\log gf$	(mÅ)	$\log \epsilon^a$	Reference ^b
O I					
6453.60	10.74	-1.288	224	7.95	NIST
6454.44	10.74	-1.066	220	7.72	NIST
7156.70	12.73	0.288	268	7.74	NIST
7950.83	12.54	0.340	382	8.03	NIST
7952.16	12.54	0.170	342	8.04	NIST
7943.15	12.54	-0.550	107	7.73	NIST
6155.98	10.69	-0.660	346	7.75	Luck
6156.77	10.69	-0.440	399	7.74	NIST
5330.66	10.69	-0.970	269	7.74	NIST
5435.78	10.74	-1.544	210	8.12	NIST
5436.86	10.74	-1.399	265	8.18	NIST
Mean:		7.89 ± 0.18			
F I					
6902.48	12.73	0.180	Synth	6.00	NIST
6909.82	12.75	-0.230	Synth	6.35	NIST
6834.26	12.73	-0.210	Synth	6.13	NIST
7331.96	12.70	-0.110	Synth	6.06	NIST
7398.69	12.70	0.240	Synth	6.00	NIST
7754.70	12.98	0.240	Synth	6.06	NIST
Mean:		6.10 ± 0.12			
Ne I					
7032.41	16.62	-0.228	286	8.71	NIST
6334.43	16.62	-0.310	321	8.82	NIST
6217.28	16.62	-0.960	207	8.68	NIST
6143.06	16.62	-0.100	336	8.64	NIST
5975.53	16.62	-1.250	145	8.46	NIST
5944.83	16.62	-0.520	249	8.44	NIST
5881.90	16.62	-0.750	215	8.43	NIST
7245.17	16.67	-0.622	269	9.08	NIST
6506.53	16.67	-0.020	326	8.64	NIST
6074.34	16.67	-0.480	245	8.44	NIST
6382.99	16.67	-0.230	283	8.54	NIST
6929.47	16.85	-0.200	271	8.69	NIST
7024.05	16.85	-1.380	72	8.34	NIST
6532.88	16.72	-0.680	212	8.59	NIST

Table B2 continued

Table B2 (continued)

Ion		W_λ			
λ (Å)	χ (eV)	$\log gf$	(mÅ)	$\log \epsilon^a$	Reference ^b
6717.04	16.85	-0.360	294	8.94	NIST
6266.50	16.72	-0.360	310	8.83	NIST
5852.49	16.85	-0.500	260	8.59	NIST
6163.59	16.72	-0.600	246	8.62	NIST
7438.90	16.72	-1.211	137	8.80	NIST
7488.87	18.38	-0.010	156	8.62	NIST
7535.77	18.38	-0.110	176	8.89	NIST
7544.04	18.38	-0.480	116	8.76	NIST
8377.61	18.56	0.670	271	8.67	NIST
6074.34	16.67	-0.480	245	8.44	NIST
Mean:				8.65 ± 0.18	
Na I					
5682.63	2.10	-0.706	179	6.33	NIST
5688.21	2.10	-0.452	257	6.36	NIST
6154.23	2.10	-1.547	74	6.65	NIST
4664.81	2.10	-1.565	70	6.67	NIST
8194.82	2.10	0.492	530	6.28	NIST
Mean:				6.46 ± 0.19	
Mg I					
4702.99	4.35	-0.440	213	6.69	NIST
5528.41	4.35	-0.498	248	6.79	NIST
Mean:				6.74 ± 0.08	
Mg II					
5923.37	12.08	-1.532	97	7.14	NIST
5943.50	12.08	-1.542	145	7.42	NIST
5464.14	12.08	-1.702	81	7.20	NIST
5460.02	12.08	-2.002	70	7.42	NIST
Mean:				7.29 ± 0.14	
Al II					
6823.48	13.07	-0.123	191	6.13	NIST
6837.14	13.08	0.097	217	6.07	NIST
7063.64	11.32	-0.368	372	6.39	NIST

Table B2 continued

Table B2 (continued)

Ion		W_λ			
λ (Å)	χ (eV)	$\log gf$	(mÅ)	$\log \epsilon^a$	Reference ^b
6231.78	13.07	0.389	287	6.04	NIST
5593.30	13.26	0.337	272	6.02	NIST
6920.34	13.26	-0.144	150	6.03	NIST
Mean:				6.12 ± 0.14	
Al III					
5696.60	15.64	0.232	84	6.05	NIST
5722.73	15.64	-0.071	80	6.32	NIST
Mean:				6.18 ± 0.13	
Si I					
7034.90	5.87	-0.880	63	7.19	GARZ
7932.20	5.96	-0.470	121	7.17	NIST
5708.44	4.93	-1.470	38	6.98	NIST
6145.08	5.61	-1.480	70	7.67	Luck
6155.22	5.62	-0.750	115	7.21	Tom97
Mean:				7.24 ± 0.26	
Si II					
6660.52	14.50	0.162	207	7.46	NIST
6665.00	14.49	-0.240	160	7.56	NIST
6671.88	14.53	0.409	282	7.67	NIST
5868.40	14.53	0.400	298	7.58	Kurucz
4621.42	12.52	-0.608	245	7.14	NIST
5706.37	14.17	-0.225	118	6.93	NIST
5632.97	14.19	-0.818	68	7.14	NIST
Mean:				7.35 ± 0.28	
P II					
6034.01	10.74	-0.220	136	5.40	NIST
6043.10	10.80	0.420	209	5.23	NIST
6503.46	10.91	-0.006	118	5.26	NIST
5344.75	10.74	-0.390	154	5.59	NIST
5499.73	10.80	-0.300	96	5.17	NIST
7845.63	11.02	-0.040	119	5.51	NIST

Table B2 continued

Table B2 (continued)

Ion		W_λ			
λ (Å)	χ (eV)	$\log gf$	(mÅ)	$\log \epsilon^a$	Reference ^b
Mean:		5.36 ± 0.17			
S I					
6748.79	7.87	-0.638	140	7.15	NIST
6757.16	7.87	-0.351	228	7.20	NIST
6052.66	7.87	-0.672	109	7.01	NIST
4694.11	6.52	-1.713	44	6.86	NIST
4695.44	6.52	-1.871	42	6.99	NIST
Mean:		7.04 ± 0.14			
S II					
5606.11	13.73	0.124	252	6.97	NIST
5664.73	13.66	-0.427	115	6.61	NIST
5428.67	13.58	-0.177	202	6.86	NIST
5453.83	13.67	0.442	300	6.88	NIST
5556.01	13.62	-1.020	64	6.73	NIST
4716.27	13.62	-0.365	163	6.74	NIST
4885.65	14.00	-0.674	120	6.94	NIST
4917.21	14.00	-0.375	130	6.72	NIST
4925.35	13.58	-0.206	220	6.93	NIST
4486.64	15.87	-0.400	40	6.74	NIST
Mean:		6.81 ± 0.12			
Ar I					
7067.22	11.55	-0.850	70	6.21	NIST
7383.98	11.62	-0.460	159	6.29	NIST
8264.52	11.83	-0.328	170	6.20	NIST
8006.16	11.62	-0.630	71	5.98	NIST
8103.69	11.62	-0.131	160	5.91	NIST
8408.21	11.83	0.073	181	5.82	NIST
8115.31	11.55	0.360	280	5.76	NIST
Mean:		5.99 ± 0.19			
Ca I					
4226.73	0.00	0.244	212	5.55	NIST
Ca II					

Table B2 continued

Table B2 (continued)

Ion		W_λ			
λ (Å)	χ (eV)	$\log gf$	(mÅ)	$\log \epsilon^a$	Reference ^b
8254.73	7.51	-0.390	296	5.61	NIST
5285.27	7.50	-1.180	122	5.83	NIST
4097.10	7.50	-1.000	127	5.76	NIST
Mean:		5.73 ± 0.11			
Sc II					
6309.90	1.50	-1.570	140	3.08	NIST
6279.76	1.50	-1.210	232	3.03	NIST
6245.63	1.51	-0.980	236	2.81	NIST
6604.60	1.36	-1.310	202	2.93	NIST
5684.19	1.51	-1.070	271	3.04	NIST
4420.66	0.62	-2.270	108	3.23	NIST
4014.48	0.32	-1.660	165	2.73	NIST
Mean:		2.98 ± 0.17			
Ti II					
6559.58	2.05	-2.019	147	3.99	NIST
6491.61	2.06	-1.793	314	4.28	NIST
6607.02	2.06	-2.790	49	4.21	NIST
7355.45	2.60	-1.916	210	4.44	NIST
7214.73	2.59	-1.750	206	4.25	NIST
5381.02	1.57	-1.921	316	4.17	NIST
5418.77	1.58	-2.002	230	4.00	NIST
4779.98	2.05	-1.370	345	4.10	NIST
4798.53	1.08	-2.679	253	4.50	NIST
4865.61	1.16	-2.788	237	4.60	NIST
4874.01	3.09	-0.805	322	4.11	NIST
4911.20	3.12	-0.609	375	4.10	NIST
5010.21	3.09	-1.291	275	4.43	NIST
4227.33	1.13	-2.236	352	4.51	NIST
4287.87	1.08	-2.020	398	4.42	NIST
4316.79	2.05	-1.577	281	4.18	NIST
4421.94	2.06	-1.663	317	4.38	NIST
4350.84	2.06	-1.735	245	4.22	NIST
4367.65	2.59	-0.862	399	4.23	NIST
4395.84	1.24	-1.928	316	4.12	NIST
4394.06	1.22	-1.784	342	4.05	NIST
4411.07	3.09	-0.667	348	4.14	NIST

Table B2 continued

Table B2 (continued)

Ion		W_λ			
λ (Å)	χ (eV)	$\log gf$	(mÅ)	$\log \epsilon^a$	Reference ^b
4518.33	1.08	-2.555	220	4.31	NIST
4524.68	1.23	-2.343	236	4.25	NIST
4544.02	1.24	-2.410	200	4.20	NIST
4568.32	1.22	-2.650	165	4.30	NIST
4529.48	1.57	-1.638	374	4.21	NIST
4609.27	1.18	-3.260	110	4.65	NIST
4636.32	1.16	-2.855	95	4.15	NIST
6513.04	4.00	-1.310	113	4.36	NIST
4158.28	5.43	-0.475	100	4.46	K88
Mean:				4.27 ± 0.17	
V II					
4528.48	2.28	-1.050	263	3.47	NIST
4564.58	2.27	-1.210	213	3.46	NIST
4600.17	2.26	-1.360	173	3.45	NIST
3977.72	1.48	-1.570	170	3.26	NIST
4036.76	1.48	-1.570	200	3.36	NIST
Mean:				3.40 ± 0.09	
Cr II					
6053.47	4.74	-2.150	193	4.88	NIST
5246.75	3.71	-2.460	210	4.66	NIST
5249.40	3.74	-2.620	223	4.88	NIST
5420.90	3.76	-2.360	211	4.59	NIST
5407.62	3.81	-2.088	265	4.53	NIST
5308.42	4.07	-1.810	359	4.73	NIST
5310.70	4.07	-2.270	296	4.97	NIST
5334.88	4.05	-1.562	383	4.55	NIST
5478.35	4.16	-1.908	369	4.91	NIST
5502.05	4.15	-1.990	311	4.78	NIST
5508.60	4.14	-2.120	330	4.97	NIST
4207.35	3.81	-2.457	220	4.87	NIST
4275.57	3.86	-1.709	358	4.66	NIST
4284.19	3.85	-1.864	351	4.78	NIST
4539.59	4.04	-2.530	243	5.11	NIST
4565.74	4.04	-2.110	271	4.79	NIST
4112.59	3.09	-3.019	123	4.63	NIST
4113.24	3.09	-2.274	234	4.32	NIST

Table B2 continued

Table B2 (continued)

Ion		W_λ			
λ (Å)	χ (eV)	$\log gf$	(mÅ)	$\log \epsilon^a$	Reference ^b
5620.63	6.46	-1.145	178	4.84	K88
5678.42	6.46	-1.238	119	4.68	K88
4901.62	6.49	-0.826	178	4.57	K88
4912.45	6.48	-0.948	212	4.81	K88
4145.77	5.32	-1.164	324	4.88	K88
4098.44	5.31	-1.470	165	4.57	K88
Mean:				4.75 ± 0.18	
Mn II					
7252.40	10.77	0.680	85	4.91	NIST
7330.58	3.71	-2.713	212	4.80	K88
7347.81	3.71	-3.184	183	5.18	K88
7353.55	3.70	-2.726	258	4.96	K88
7415.80	3.71	-2.202	343	4.72	NIST
7432.29	3.71	-2.498	221	4.63	NIST
6122.43	10.18	0.950	225	4.94	NIST
5295.40	9.86	0.360	217	5.28	NIST
5296.97	9.86	0.620	237	5.11	NIST
5302.32	9.86	1.000	313	5.06	NIST
5559.05	6.18	-1.318	151	4.64	NIST
4727.86	5.37	-2.017	139	4.86	K88
4755.73	5.40	-1.242	300	4.71	K88
4730.38	5.37	-2.147	132	4.96	NIST
4206.37	5.40	-1.540	189	4.67	NIST
4259.19	5.40	-1.440	233	4.72	NIST
4238.78	1.83	-3.626	248	4.85	NIST
4377.74	5.44	-2.144	61	4.61	NIST
4105.00	6.13	-1.349	170	4.82	NIST
4136.94	6.14	-1.290	151	4.67	NIST
Mean:				4.85 ± 0.19	
Fe I					
5383.37	4.31	0.645	224	6.73	NIST
5424.07	4.32	0.520	176	6.69	FMW
5615.64	3.33	0.050	135	6.40	NIST
4891.49	2.85	-0.112	136	6.32	NIST
4903.31	2.88	-0.926	55	6.67	NIST
4918.99	2.86	-0.342	149	6.61	NIST

Table B2 continued

Table B2 (continued)

Ion		W_λ			
λ (Å)	χ (eV)	$\log gf$	(mÅ)	$\log \epsilon^a$	Reference ^b
5162.29	4.16	0.020	82	6.67	NIST
4920.50	2.83	0.068	338	6.83	NIST
Mean:				6.61 ± 0.17	
Fe II					
6386.75	6.77	-2.600	140	6.78	NIST
6487.43	6.78	-2.500	156	6.77	NIST
6770.90	11.20	-0.360	120	6.89	NIST
6792.54	11.22	-0.110	98	6.52	NIST
6857.85	11.22	0.610	234	6.53	NIST
6932.00	11.31	0.400	175	6.52	NIST
6927.88	11.26	0.670	235	6.51	NIST
7301.56	3.89	-4.000	185	6.74	NIST
7417.54	5.82	-3.486	84	6.87	NIST
7496.69	11.08	-0.610	43	6.53	NIST
7506.54	9.74	-0.420	201	6.63	NIST
7690.51	9.78	-0.260	241	6.68	NIST
7780.37	9.76	-0.400	218	6.70	NIST
7801.25	5.90	-2.900	143	6.64	NIST
7548.66	11.30	0.090	137	6.67	NIST
7543.38	11.35	-0.540	75	6.91	NIST
7688.45	11.08	-0.070	149	6.77	NIST
7748.36	11.05	-0.090	161	6.84	NIST
7739.16	11.11	-0.900	21	6.49	NIST
7969.04	11.35	-0.640	89	7.10	NIST
7718.51	11.30	-0.180	124	6.86	NIST
7829.73	7.52	-2.130	110	6.63	NIST
7851.94	6.23	-2.700	160	6.71	NIST
7866.56	5.55	-3.321	89	6.57	NIST
7981.91	9.65	-0.560	180	6.60	NIST
5627.49	3.39	-4.080	233	6.68	NIST
5725.95	3.42	-4.800	157	7.14	NIST
5907.37	7.81	-2.300	110	6.88	NIST
5648.90	10.56	-0.170	240	6.85	NIST
5726.55	10.71	-0.040	177	6.52	NIST
5746.57	10.63	-0.400	186	6.87	NIST
5751.49	10.63	-0.610	115	6.72	NIST
5838.99	10.84	-0.600	106	6.77	NIST
5871.77	10.83	-0.280	191	6.88	NIST

Table B2 continued

Table B2 (continued)

Ion		W_λ			
λ (Å)	χ (eV)	$\log gf$	(mÅ)	$\log \epsilon^a$	Reference ^b
5842.29	10.74	-0.330	201	6.93	NIST
5891.36	7.24	-2.030	247	6.90	NIST
5948.42	10.74	-0.200	214	6.87	NIST
5965.62	10.68	0.070	244	6.71	NIST
5976.68	10.68	-0.330	164	6.74	NIST
5981.75	7.87	-2.200	80	6.64	NIST
6060.97	7.80	-1.690	200	6.69	NIST
6049.44	10.71	-0.370	159	6.78	NIST
6229.34	2.82	-4.824	121	6.64	NIST
5241.05	10.39	-0.580	239	7.14	NIST
5218.84	10.38	-0.170	242	6.74	NIST
5257.89	10.46	-0.530	192	6.91	NIST
5245.45	10.46	-0.540	210	7.01	NIST
5228.89	10.45	-0.300	203	6.73	NIST
5222.35	10.52	-0.280	140	6.45	NIST
5311.91	10.54	-1.020	89	6.91	NIST
5315.08	10.54	-0.420	166	6.72	NIST
5351.93	10.50	-1.110	118	7.15	NIST
5405.66	10.52	-0.440	217	6.98	NIST
5399.56	10.52	-0.750	105	6.73	NIST
5375.84	10.45	-0.330	247	6.97	NIST
5443.44	10.48	-0.600	194	7.01	NIST
5388.03	10.45	-0.690	121	6.73	NIST
5445.80	10.54	-0.110	224	6.70	NIST
5479.40	10.56	-0.350	205	6.86	NIST
5444.39	10.60	-0.170	228	6.81	NIST
5451.32	10.50	-0.650	196	7.08	NIST
5532.09	10.52	-0.100	217	6.65	NIST
5488.78	10.60	-0.400	157	6.71	NIST
5548.23	10.62	-0.540	223	7.17	NIST
5563.39	10.63	-0.550	129	6.73	NIST
5571.52	10.60	-1.060	105	7.09	NIST
4866.20	10.31	-0.670	157	6.80	NIST
4833.19	2.66	-4.800	160	6.75	NIST
4839.99	2.68	-4.900	190	6.97	NIST
4869.97	10.35	-1.540	35	6.85	NIST
4838.55	10.33	-1.700	47	7.14	NIST
4893.78	2.83	-4.300	246	6.65	NIST
4946.90	10.35	-1.500	56	7.04	NIST
4971.22	10.36	-0.500	202	6.87	NIST

Table B2 continued

Table B2 (continued)

Ion		W_λ			
λ (Å)	χ (eV)	$\log gf$	(mÅ)	$\log \epsilon^a$	Reference ^b
4948.09	10.31	-0.220	206	6.58	NIST
4977.03	10.36	-0.040	244	6.61	NIST
4958.82	10.38	-0.760	146	6.88	NIST
5029.09	10.36	-0.630	210	7.04	NIST
4977.92	10.23	-0.600	149	6.66	NIST
5065.11	10.43	-0.550	198	6.94	NIST
5106.11	10.33	-0.250	194	6.57	NIST
5006.84	10.38	-0.360	196	6.71	NIST
5060.25	10.45	-0.650	136	6.76	NIST
5094.90	10.47	-0.720	138	6.85	NIST
5115.06	10.43	-0.500	160	6.72	NIST
5141.38	10.47	-0.770	174	7.07	NIST
5180.31	10.39	-0.090	212	6.53	NIST
5199.12	10.38	0.120	246	6.47	NIST
5223.26	10.39	-0.170	203	6.57	NIST
5186.87	10.47	-0.190	159	6.43	NIST
5219.92	10.52	-0.550	136	6.70	NIST
4598.49	7.80	-1.540	242	6.73	NIST
4601.34	2.88	-4.430	220	6.75	NIST
6362.47	10.91	-0.490	182	7.15	NIST
6375.80	10.93	-0.010	184	6.69	NIST
6548.39	11.02	0.240	197	6.58	NIST
6541.37	11.05	0.350	192	6.46	NIST
6650.98	7.13	-2.400	115	6.68	NIST
6357.16	10.91	0.240	217	6.59	NIST
7616.93	11.27	-0.820	98	7.32	NIST
Mean:				6.78 ± 0.19	
Co II					
4516.65	3.46	-2.460	156	4.66	NIST
4569.26	3.41	-2.400	183	4.68	NIST
4660.65	3.36	-2.350	242	4.81	NIST
Mean:				4.72 ± 0.08	
Ni I					
4904.41	3.54	-0.170	25	5.47	NIST
5081.11	3.85	0.300	50	5.49	NIST
4714.42	3.38	0.230	66	5.45	NIST

Table B2 continued

Table B2 (continued)

Ion		W_λ			
λ (Å)	χ (eV)	$\log gf$	(mÅ)	$\log \epsilon^a$	Reference ^b
Mean:				5.47 ± 0.02	
Ni II					
4192.07	4.01	-3.060	254	5.58	K88
5003.41	12.54	0.702	105	5.55	K88
Mean:				5.56 ± 0.03	
Ge II					
7049.37	8.08	0.000	Synth	3.60	NIST
7145.39	8.06	-0.300	Synth	3.77	NIST
6021.04	7.74	-0.040	Synth	3.80	NIST
Mean:				3.72 ± 0.09	
Sr II					
4215.52	0.00	-0.166	716	3.39	NIST
4077.71	0.00	0.148	707	3.12	NIST
4305.45	3.04	-0.100	360	3.55	NIST
4161.80	2.94	-0.470	270	3.56	NIST
Mean:				3.40 ± 0.20	
Y II					
5728.89	1.84	-1.120	62	2.73	NIST
5402.77	1.84	-0.510	220	2.84	NIST
4786.58	1.03	-1.290	110	2.74	NIST
4854.86	0.99	-0.380	314	2.49	NIST
4900.12	1.03	-0.090	370	2.38	NIST
5087.42	1.08	-0.170	402	2.56	NIST
5205.72	1.03	-0.350	318	2.45	NIST
4309.62	0.18	-0.747	257	2.24	NIST
4398.01	0.13	-0.999	280	2.51	NIST
4682.32	0.41	-1.509	130	2.66	NIST
3950.35	0.10	-0.488	370	2.39	NIST
5662.92	1.94	0.160	324	2.51	NIST
Mean:				2.54 ± 0.17	

Table B2 continued

Table B2 (*continued*)

Ion		W_λ		$\log \epsilon^a$	Reference ^b
λ (Å)	χ (eV)	$\log gf$	(mÅ)		
Zr II					
4208.99	0.71	-0.510	386	2.79	Ljung
4359.74	1.24	-0.510	261	2.68	Ljung
4440.45	1.21	-1.040	238	3.11	Ljung
4495.44	1.21	-1.830	75	3.21	Ljung
4379.78	1.53	-0.356	334	2.95	CC
4308.94	1.49	-0.800	142	2.73	Kurucz
4494.41	2.41	-0.230	290	3.22	Malcheva
4496.96	0.71	-0.890	270	2.72	Ljung
4613.95	0.97	-1.540	156	3.15	Ljung
4661.78	2.41	-0.800	115	3.15	Kurucz
3998.98	0.56	-0.520	410	2.86	Ljung
4050.32	0.71	-1.060	250	2.91	Ljung
4156.24	0.71	-0.780	270	2.67	Ljung
4211.88	0.53	-1.040	340	3.03	Ljung
4018.38	0.96	-1.270	137	2.88	Ljung
5350.10	1.83	-0.390	261	2.81	Ljung
Mean:				2.93 ± 0.19	
Ba II					
6141.71	0.70	-0.032	350	2.35	NIST
6496.90	0.60	-0.407	280	2.45	NIST
4934.08	0.00	-0.160	302	2.00	NIST
4554.03	0.00	0.140	409	2.12	NIST
Mean:				2.23 ± 0.21	

^aNormalized such that $\log \sum \mu_i \epsilon(i) = 12.15$.

^bSources of $\log gf$ values.

References—NIST: [Kramida et al. \(2023\)](#); K88: [Kurucz \(1988\)](#); CC: [Cowley & Corliss \(1983\)](#); FMW: [Fuhr et al. \(1988\)](#); GARZ: [Garz \(1973\)](#); Luck: Compilations by R. E. Luck; Tom97: [Tomkin et al. \(1997\)](#); KP: [Kurucz & Peytremann \(1975\)](#); NBS: [Wiese et al. \(1966\)](#); Kurucz: Kurucz Database; Malcheva: [Malcheva et al. \(2006\)](#); Ljung: [Ljung et al. \(2006\)](#)

C. SPECTRUM SYNTHESIS OF HYDROGEN LINE

The available hydrogen Balmer lines ($H\alpha$, $H\beta$, and $H\gamma$) are synthesized to obtain the hydrogen abundance ($\log \epsilon(H)$). For example, synthesis of the $H\alpha$ line is shown in Figure C1. The hydrogen Balmer lines are synthesized using the optimum model atmosphere with

$T_{\text{eff}} = 9250$ K, $\log g = 1.25$ cgs and $\xi = 11.5$ km s⁻¹, and C/He=0.3 %.

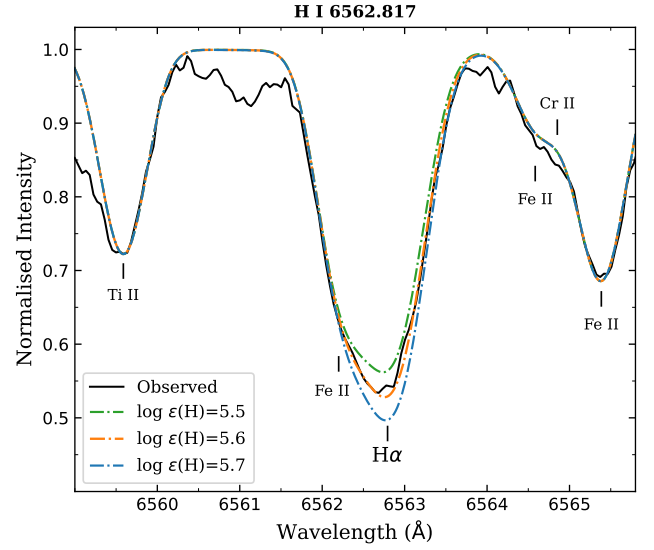


Figure C1. Observed and synthesized $H\alpha$ line profile is shown for A 980.

REFERENCES

- Asplund, M., Grevesse, N., Sauval, A. J., & Scott, P. 2009, *ARA&A*, 47, 481, doi: [10.1146/annurev.astro.46.060407.145222](https://doi.org/10.1146/annurev.astro.46.060407.145222)
- Asplund, M., Gustafsson, B., Kiselman, D., & Eriksson, K. 1997, *A&A*, 318, 521
- Bhowmick, A., Pandey, G., & Lambert, D. L. 2020, *ApJ*, 891, 40, doi: [10.3847/1538-4357/ab6e6d](https://doi.org/10.3847/1538-4357/ab6e6d)
- Bidelman, W. P. 1953, *ApJ*, 117, 25, doi: [10.1086/145665](https://doi.org/10.1086/145665)
- Biehle, G. T. 1994, *ApJ*, 420, 364, doi: [10.1086/173566](https://doi.org/10.1086/173566)
- Clayton, G. C. 1996, *PASP*, 108, 225, doi: [10.1086/133715](https://doi.org/10.1086/133715)
- Cowley, C. R., & Corliss, C. H. 1983, *MNRAS*, 203, 651, doi: [10.1093/mnras/203.3.651](https://doi.org/10.1093/mnras/203.3.651)
- Dimitrijevic, M. S., & Sahal-Brechot, S. 1984, *JQSRT*, 31, 301, doi: [10.1016/0022-4073\(84\)90092-X](https://doi.org/10.1016/0022-4073(84)90092-X)
- Drilling, J. S., Jeffery, C. S., & Heber, U. 1998, *A&A*, 329, 1019
- Farmer, R., Renzo, M., Götberg, Y., et al. 2023, *MNRAS*, 524, 1692, doi: [10.1093/mnras/stad1977](https://doi.org/10.1093/mnras/stad1977)
- Fuhr, J. R., Martin, G. A., & Wiese, W. L. 1988, *Journal of Physical and Chemical Reference Data*, 17
- Garz, T. 1973, *A&A*, 26, 471
- Goswami, A., & Prantzos, N. 2000, *A&A*, 359, 191, doi: [10.48550/arXiv.astro-ph/0005179](https://doi.org/10.48550/arXiv.astro-ph/0005179)
- Hema, B. P., Pandey, G., & Lambert, D. L. 2012, *ApJ*, 747, 102, doi: [10.1088/0004-637X/747/2/102](https://doi.org/10.1088/0004-637X/747/2/102)
- Hubeny, I., Hummer, D. G., & Lanz, T. 1994, *A&A*, 282, 151
- Hubeny, I., & Lanz, T. 2017, arXiv e-prints, arXiv:1706.01859, doi: [10.48550/arXiv.1706.01859](https://doi.org/10.48550/arXiv.1706.01859)
- Jeffery, C. S. 1998, *MNRAS*, 294, 391
- . 2017, *MNRAS*, 470, 3557, doi: [10.1093/mnras/stx1442](https://doi.org/10.1093/mnras/stx1442)
- Jeffery, C. S., Hamill, P. J., Harrison, P. M., & Jeffers, S. V. 1998, *A&A*, 340, 476
- Jeffery, C. S., & Heber, U. 1992, *A&A*, 260, 133
- Jeffery, C. S., Scott, L. J. A., Philip Monai, A., Miszalski, B., & Woolf, V. M. 2024, *MNRAS*, 530, 1666, doi: [10.1093/mnras/stae961](https://doi.org/10.1093/mnras/stae961)
- Karakas, A. I., Lugaro, M., Carlos, M., et al. 2018, *MNRAS*, 477, 421, doi: [10.1093/mnras/sty625](https://doi.org/10.1093/mnras/sty625)
- Karakas, A. I., Lugaro, M., & Gallino, R. 2007, *ApJL*, 656, L73, doi: [10.1086/512676](https://doi.org/10.1086/512676)
- Kramida, A., Ralchenko, Y., Reader, J., & Team(2023), N. A. 2023, NIST Atomic Spectra Database (version 5.11), doi: [10.18434/T4W30F](https://doi.org/10.18434/T4W30F)
- Kurucz, R. 1988, in *Trans. IAU, Vol. XXB, Transactions of the International Astronomical Union*, ed. M. McNally (Dordrecht: Kluwer), 168–172
- Kurucz, R. L., & Peytremann, E. 1975, *SAO Special Report*
- Ljung, G., Nilsson, H., Asplund, M., & Johansson, S. 2006, *A&A*, 456, 1181, doi: [10.1051/0004-6361:20065212](https://doi.org/10.1051/0004-6361:20065212)
- Malcheva, G., Blagoev, K., Mayo, R., et al. 2006, *MNRAS*, 367, 754, doi: [10.1111/j.1365-2966.2005.09987.x](https://doi.org/10.1111/j.1365-2966.2005.09987.x)
- Menon, A., Karakas, A. I., Lugaro, M., Doherty, C. L., & Ritter, C. 2019, *MNRAS*, 482, 2320, doi: [10.1093/mnras/sty2606](https://doi.org/10.1093/mnras/sty2606)
- Moore, C. E. 1972, A multiplet table of astrophysical interest, revised edition ::part I - table of multiplets, part II - finding list of all lines in the table of multiplets, , National Institute of Standards and Technology, Gaithersburg, MD, doi: <https://doi.org/10.6028/NBS.NSRDS.40>
- . 1993, *Tables of Spectra of Hydrogen, Carbon, Nitrogen, and Oxygen Atoms and Ions (Evaluated Data in Atomic Physics)*, ed. J. W. Gallagher (Boca Raton: CRC Press)
- Pandey, G. 2006, *ApJL*, 648, L143, doi: [10.1086/507888](https://doi.org/10.1086/507888)
- Pandey, G., Hema, B. P., & Reddy, A. B. S. 2021, *ApJ*, 921, 52, doi: [10.3847/1538-4357/ac1ad1](https://doi.org/10.3847/1538-4357/ac1ad1)
- Pandey, G., Kameswara Rao, N., Jeffery, C. S., & Lambert, D. L. 2014, *ApJ*, 793, 76, doi: [10.1088/0004-637X/793/2/76](https://doi.org/10.1088/0004-637X/793/2/76)
- Pandey, G., Kameswara Rao, N., Lambert, D. L., Jeffery, C. S., & Asplund, M. 2001, *MNRAS*, 324, 937, doi: [10.1046/j.1365-8711.2001.04371.x](https://doi.org/10.1046/j.1365-8711.2001.04371.x)
- Pandey, G., & Lambert, D. L. 2011, *ApJ*, 727, 122, doi: [10.1088/0004-637X/727/2/122](https://doi.org/10.1088/0004-637X/727/2/122)
- . 2017, *ApJ*, 847, 127, doi: [10.3847/1538-4357/aa88bb](https://doi.org/10.3847/1538-4357/aa88bb)
- Pandey, G., Lambert, D. L., Jeffery, C. S., & Rao, N. K. 2006, *ApJ*, 638, 454, doi: [10.1086/498674](https://doi.org/10.1086/498674)
- Pandey, G., Lambert, D. L., Rao, N. K., & Jeffery, C. S. 2004, *ApJL*, 602, L113, doi: [10.1086/382684](https://doi.org/10.1086/382684)
- Pandey, G., & Reddy, B. E. 2006, *MNRAS*, 369, 1677, doi: [10.1111/j.1365-2966.2006.10398.x](https://doi.org/10.1111/j.1365-2966.2006.10398.x)
- Przybilla, N., Fossati, L., & Jeffery, C. S. 2021, *Research Notes of the American Astronomical Society*, 5, 254, doi: [10.3847/2515-5172/ac342a](https://doi.org/10.3847/2515-5172/ac342a)
- Roederer, I. U. 2012, *ApJ*, 756, 36, doi: [10.1088/0004-637X/756/1/36](https://doi.org/10.1088/0004-637X/756/1/36)
- Ryde, N., & Lambert, D. L. 2004, *A&A*, 415, 559, doi: [10.1051/0004-6361:20034616](https://doi.org/10.1051/0004-6361:20034616)
- Shultz, M. E., Kochukhov, O., Labadie-Bartz, J., David-Uraz, A., & Owocki, S. P. 2021, *MNRAS*, 507, 1283, doi: [10.1093/mnras/stab2162](https://doi.org/10.1093/mnras/stab2162)
- Tisserand, P., Crawford, C. L., Clayton, G. C., et al. 2022, *A&A*, 667, A83, doi: [10.1051/0004-6361/202142916](https://doi.org/10.1051/0004-6361/202142916)

- Tody, D. 1986, in Society of Photo-Optical Instrumentation Engineers (SPIE) Conference Series, Vol. 627, Instrumentation in astronomy VI, ed. D. L. Crawford, 733, doi: [10.1117/12.968154](https://doi.org/10.1117/12.968154)
- Tody, D. 1993, in Astronomical Society of the Pacific Conference Series, Vol. 52, Astronomical Data Analysis Software and Systems II, ed. R. J. Hanisch, R. J. V. Brissenden, & J. Barnes, 173
- Tomkin, J., Edvardsson, B., Lambert, D. L., & Gustafsson, B. 1997, *A&A*, 327, 587, doi: [10.48550/arXiv.astro-ph/9707208](https://doi.org/10.48550/arXiv.astro-ph/9707208)
- Warner, B. 1963, *MNRAS*, 126, 61, doi: [10.1093/mnras/126.1.61](https://doi.org/10.1093/mnras/126.1.61)
- . 1967, *MNRAS*, 137, 119, doi: [10.1093/mnras/137.2.119](https://doi.org/10.1093/mnras/137.2.119)
- Wiese, W. L., Smith, M. W., & Glennon, B. M. 1966, Atomic transition probabilities. Vol.: Hydrogen through Neon. A critical data compilation, NSRDS-NBS 4